CSIRO PUBLISHING

COLLECTION | RESEARCH PAPER
https://doi.org/10.1071/WF24163

International Journal of WILDLAND FIRE

International Association of Wildland Fire

Mobile radar provides insights into hydrologic responses in burn areas

Jonathan J. Gourley[A,*], Yagmur Derin[B,C], Pierre-Emmanuel Kirstetter[B,A], John W. Fulton[D], Laura A. Hempel[D] and Braden White[E,A]

For full list of author affiliations and declarations see end of paper

***Correspondence to:**
Jonathan J. Gourley
NOAA/National Severe Storms Laboratory, Norman, OK, USA
Email: jj.gourley@noaa.gov

Received: 27 September 2024
Accepted: 22 April 2025
Published: 26 May 2025

Cite this: Gourley JJ *et al.* (2025) Mobile radar provides insights into hydrologic responses in burn areas. *International Journal of Wildland Fire* **34**, WF24163. doi:10.1071/WF24163

ABSTRACT

Background. Wildfires often occur in mountainous terrain, regions that pose substantial challenges to operational meteorological and hydrologic observing networks. **Aims.** A mobile, post-fire hydrometeorological observatory comprising remote-sensing and *in situ* instrumentation was developed and deployed in a burnt area to provide unique insights into rainfall-induced post-fire hazards. **Methods.** Mobile radar-based rainfall estimates were produced throughout the burn area at 75-m resolution and compared with rain gauge accumulations and basin response variables. **Key results.** The mobile radar was capable of resolving details in intra-basin rain fields as well as detecting storms approaching the burn area with accuracy equivalent to rain gauges. Runoff responses were complex and dependent on spatiotemporal patterns and magnitude of rainfall intensity over the burn area. **Conclusions.** The complement of the mobile radar with the near-field, non-contact instruments measuring the hydrologic response provided valuable information in regions that are difficult to access and are not routinely monitored by conventional observing networks. **Implications.** Post-fire observatories equipped with mobile radars deployed on burn areas provide real-time data, early alerting capabilities and visualizations to potentially guide impact-based decision support for local authorities.

Keywords: debris flows, extreme hydrologic response, mobile observatory, post-fire hazards, rainfall estimation, remote sensing, Rocky Mountains, stream radar, weather radar.

Introduction

Wildfires produce direct and immediate impacts on communities in terms of property damage, air and water quality degradation, and ecology (Neary and Leonard 2019). Even after a wildfire is contained, it continues to pose a longer-lasting hazard through rainfall that produces hydrologic responses such as flash flooding, severe erosion and debris flows (Moody *et al.* 2013). Numerous studies have found that wildfires have been increasing in terms of frequency, duration, intensity and size in the western United States (US) and will continue to do so because of climate change (Abatzoglou and Williams 2006; Westerling *et al.* 2006; Dennison *et al.* 2014; Parks and Abatzoglou 2020). Thus, it may be useful to develop and employ new observational, modeling and alerting strategies to mitigate the community impacts from rainfall-triggered geomorphological and hydrologic hazards originating from burnt areas.

Routine operational meteorological and hydrologic observing networks often fail to adequately monitor these post-fire hydrologic responses. Burn areas are frequently found in mountainous regions where substantial radar beam blockages by surrounding terrain impede low-level coverage by the WSR-88D radar network (Maddox *et al.* 2002). Fig. 1 shows the height of the lowest beam (above ground level (AGL)) that is not blocked by terrain by more than 50% and reveals expansive regions (e.g. northeastern Arizona, southern Nevada, southern Oregon) that do not have coverage below 3 km AGL, which is

Collection: Establishing Directions in Postfire Debris-Flow Science

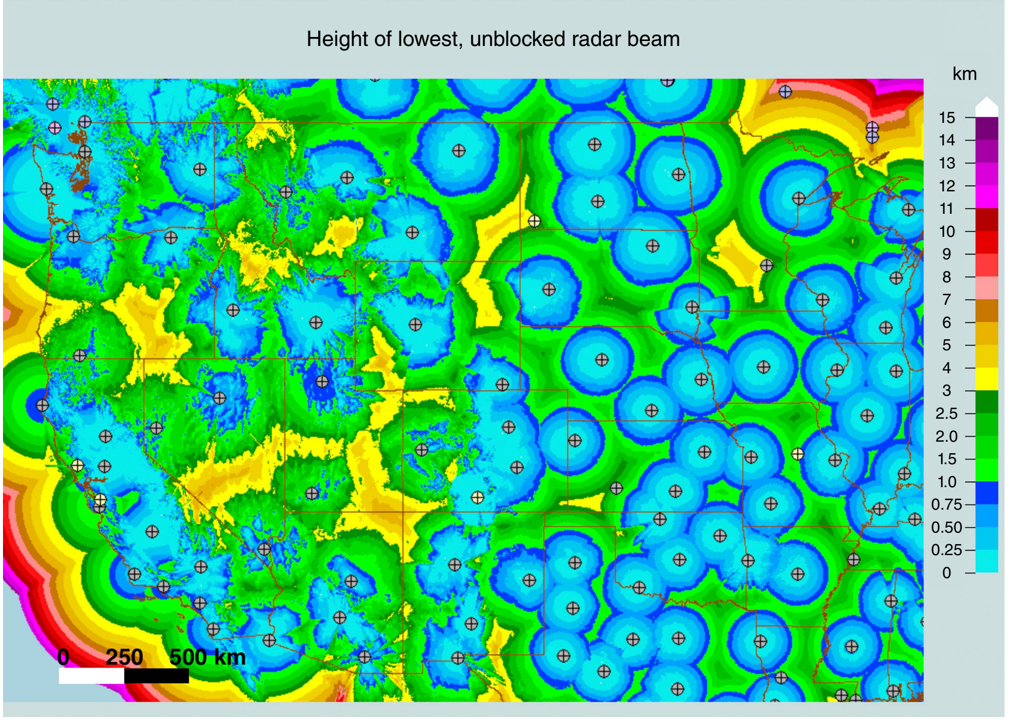

Fig. 1. Height above ground level (in km) of unblocked radar beams from operational weather radars in the United States and Canada (NOAA Multi-Radar/Multi-Sensor System (MRMS) 2024).

a threshold height considered necessary for accurate rainfall estimation and severe weather identification (Maddox *et al.* 2002). Those regions that do have high-quality radar coverage often lack the spatial resolution needed for resolving fine-scale rainfall variability within small headwater catchments, which needs to be resolved for initiating post-fire responses. At a range of 100 km, the width of the radar beam is 1.6 km, indicating that rainfall variability cannot be resolved within basins smaller than 2.6 km^2. Rain gauge networks can be deployed and utilized, but they are limited in terms of their spatial representativeness of rain fields, and they have their own sources of error, such as undercatch owing to wind effects (Alter 1937; Habib *et al.* 2001). In terms of hydrologic observation, the US Geological Survey (USGS) operates and maintains a network of more than 10,000 streamgages throughout the country (Eberts *et al.* 2018). More than 70% of the streamgages are placed on streams with catchments larger than 100 km^2; few are in regions impacted by wildfire owing to difficulties with access, power and communications (Krabbenhoft *et al.* 2022). Lack of dense rain gauge and streamgage observations may limit the ability of local National Weather Service (NWS) forecasters to recognize an impending disaster and to provide early alerts to the public and local communities. The inadequacies of conventional observing networks to provide early alert functionality in a potentially vulnerable environment motivated the development of a suite of *in situ*, non-contact and remote-sensing instruments to act as multiple lines of defense for observing rainfall and extreme hydrologic responses. This work builds on prior efforts that have supplemented rain gauges using mobile weather radars for supporting post-fire flood and debris flow warnings in steep, mountainous terrain (NOAA-USGS Debris Flow Task Force 2005; Jorgensen *et al.* 2011).

Federal, state and local partners coordinated to establish a mobile post-fire hydrometeorological observatory located in the mountainous Spring Creek burn area in southeastern Colorado (CO), US, beginning in 2019. This article documents the instruments comprising the observatory, details the processing steps to provide accurate rainfall estimates from mobile radar and reveals insights into rainfall runoff behavior and debris flow initiation using non-contact stream velocity and stage radars. Recommendations for observatory configuration, design and instrumentation are provided to potentially extend the capabilities from a research platform to a real-time decision support system for local and federal authorities.

Materials and methods

Study site background

The Spring Creek Fire was ignited by an illegal campfire on 27 June 2018 east of Fort Garland, CO, and advanced to the western flank of the Sangre de Cristo foothills (Fig. 2). It continued to burn throughout the summer and was not fully

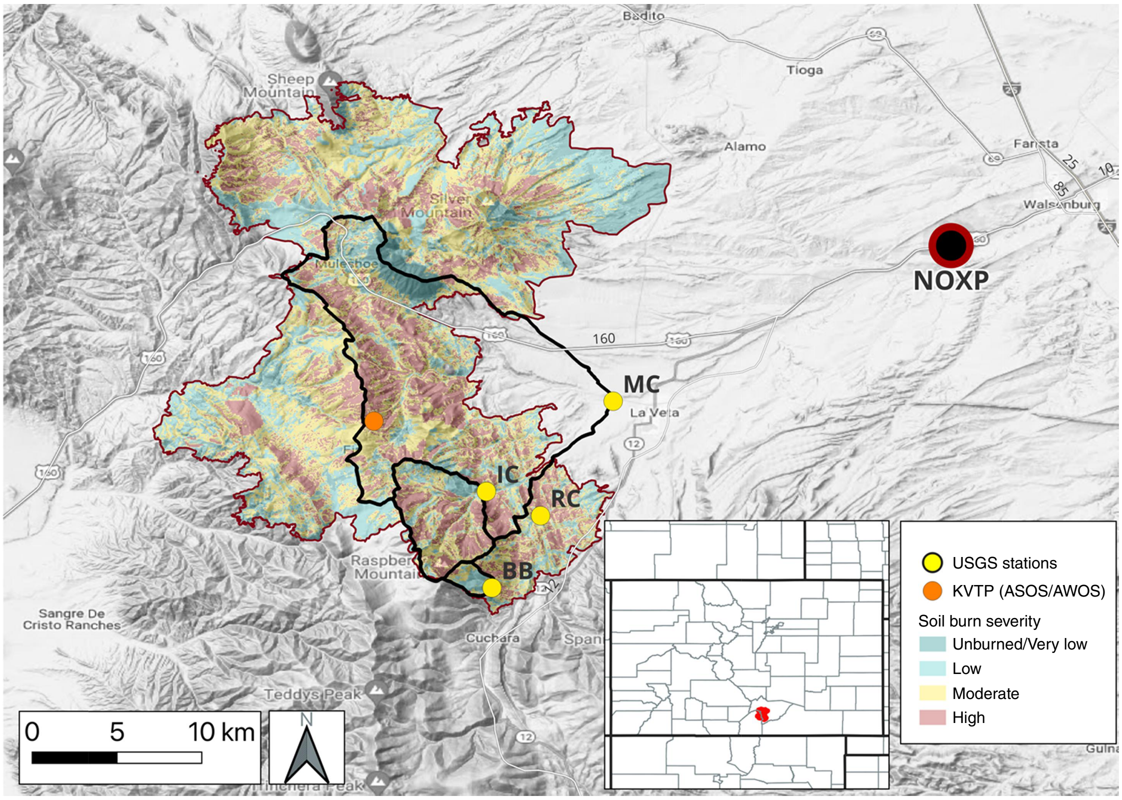

Fig. 2. Study domain showing the location of the NOAA mobile weather X-band radar with dual-polarimetric capabilities (NOXP) (black dot with red outline), the Spring Creek burn area with colors corresponding to soil burn severity (red outline) (MTBS 2020), the Automated Surface/Weather Observing Systems (ASOS/AWOS) station operated on top of La Veta Pass (KVTP) (orange dot) (National Weather Service 2025), and the US Geological Survey (USGS)-gaged basin outlets (yellow dots) (US Geological Survey 2020). Basin outlets for Middle Creek (MC), Indian Creek (IC), Rilling Creek (RC) and Big Branch Creek (BB) are shown.

contained until 10 September 2018. A total of 437 km^2 (108,045 acres) of forested foothills and mountains was burned, destroying 141 structures, and costing more than US$32 million in resources to contain (Colorado Encyclopedia 2020). At the time of the fire, it was the third largest fire in the state's history. A Burned Area Emergency Response (BAER) team was rapidly deployed to the burn area following containment to assess the condition of the landscape. The post-fire soil burn severity (SBS) map was created by the BAER team using standard procedures documented in the US Forest Service field guide (Parsons *et al.* 2010; MTBS 2020). Fig. 2 shows the extent of the SBS assessment, ranging from unburned/very low to high severity. Approximately 65% of the burn area was assessed as having either moderate or high SBS.

During the next year (2019), the CO Department of Transportation developed an Emergency Response Plan given the high likelihood of flooding and debris flow impacts to nearby highways. The document provides a detailed state response plan to monitor and potentially close local highways following the issuance of a flash flood warning by the local NWS office in Pueblo, CO. The most immediate concerns were US Highway 160 and State Highways 12 and 69 (Fig. 2). The latter two have been designated a Scenic and Historic Byway as part of the Highway of Legends (Highway of Legends 2024). These highways experience a substantial increase in traffic during the summer months because of proximity to populations in the surrounding plains where hot summer temperatures are common. Many of the tourists who are seeking cooler temperatures and mountain views may be unfamiliar with the region and are unaware of any vulnerabilities to post-fire hazards. The streams and creeks emanating from the burn area drain east and south to the tourist towns of La Veta and Cuchara, CO. The population of both towns combined is less than 1000 (United States Census Bureau 2020) but they experience a significant uptick in visitors during the summer months.

USGS instruments

The location of USGS instruments comprising the post-fire hydrometeorological observatory is illustrated in Fig. 2, and the data inventory is summarized in Table 1. The USGS stations included one or more of the following instruments

Table 1. Inventory of data collection for the Spring Creek burn area, CO, USA (US Geological Survey 2020; Hempel *et al.* 2025; Gourley 2024, 2025).

Owner	Site ID	Site name	Location	Basin area (km^2)	Variables	Dates active
USGS	373044105015701[A]	Middle Creek	37.5123, -105.0325	175.3	Stream stage,[B] stream velocity[B]	2019–2021 2019–2021
USGS	372742105061301[A]	Indian Creek	37.4616, -105.1037	24.7	Stream velocity,[B] precipitation,[B] soil moisture[B]	2019–2020 2019–2021 2019–2021
USGS	372653105042401[A]	Rilling Creek	37.4480, -105.0733	2.1	Stream stage,[B] stream velocity,[B] precipitation,[B] soil moisture[B]	2019–2020 2019–2020 2019–2020
USGS	372427105060201[A]	Big Branch	37.4075, -105.1006	3.1	Stream stage,[B] stream velocity,[B] precipitation,[B] soil moisture[B]	2019–2020 2019–2021 2019–2021
NOAA	NOXP radar[C]	Lathrop State Park	37.5997, -104.8425	N/A	Reflectivity, differential reflectivity, radial velocity, correlation coefficient, differential phase shift	2019–2021 2019–2021 2019, 2021

[A]US Geological Survey (2020).
[B]Hempel *et al.* (2025).
[C]Gourley (2025).

located at Big Branch Creek, Indian Creek, Middle Creek and Rilling Creek: trail cameras, tipping bucket rain gauges, velocity and stage non-contact radars, and soil moisture probes. The trail cameras provided still photos every 10–15 min for monitoring situational awareness. The tipping bucket rain gauges were HyQuest Solutions' TB6 models that had a reporting frequency of 15 min and each tip corresponded to 0.254 mm (HyQuest Solutions 2018). The rain gauges were mounted to steel pipes and affixed to opportunistic structures such as tree stumps. They were calibrated to within $\pm 5\%$ at both the beginning and end of the seasonal field deployments (USGS 2009). USGS technicians calibrated single tips using a pipette with the volume of water corresponding to the minimum data resolution of 0.254 mm (USGS 2009). They also checked the rainfall intensity of at least 50.8 mm h^{-1} by steadily introducing the corresponding volume of water to each gauge. An Automated Surface/Weather Observing Systems (ASOS/AWOS) station operated by the NWS was available in Middle Creek on top of La Veta Pass (KVTP) (National Weather Service 2025). The calibration standards and data quality from this gauge are not quantified as with the USGS stations, and the data were incorporated and used as is.

The USGS used non-contact radars for quantifying stream stage and/or velocity. These radar units were manufactured by SOMMER Messtechnik, and the models were either RQ-30 (stage and velocity) or RG-30 (velocity). A detailed description of the RQ-30 units, including a quantification of their errors, is provided in Khan *et al.* (2021). The non-contact stream radars were either suspended above the thalweg of streams by connecting cables to trees, or they were mounted to trees using a cantilever design. Data loggers and 12 V batteries were all housed in a waterproof case that was mounted near the instruments. Batteries were charged using solar panels. Data were transmitted in real time using redundant modes of telemetry including cellular, Geostationary Operational Environmental Satellite (GOES) and Iridium satellites. In some cases, data were telemetered using a radio to a nearby site on a ridge with better cellular reception. The data loggers were equipped with alerting capabilities; user-defined thresholds on radar stage and velocity were set, and if they were exceeded, the logging intervals would decrease from 15 to 1 min. In 2020–2021, stream velocity and stage were collected at 1-min intervals by default. Precipitation data were all logged and transmitted every 15 min for the duration of the experiment (Hempel *et al.* 2025).

National Oceanic and Atmospheric Administration (NOAA) mobile radar – NOXP

To quantify rainfall at high spatial resolution through remote-sensing methods, we deployed the NOXP radar system. NOXP is a mobile, X-band radar with dual-polarimetric capabilities. It was sited at Lathrop State Park, CO, where it was powered by an onboard diesel generator (Supplementary material Fig. S1). This location is 22.5–41.5 km from the nearest and farthest points of the gaged basins on the burn area. It operates at 9415 MHz, which corresponds to a 3-cm wavelength (X band). The peak power is 250 kW, and the beamwidth is 0.9°. The radar transmitter was configured with a pulse width of 0.5 μs, which results in a range gate spacing of 75 m, and a pulse repetition frequency of 1000 Hz, resulting in a maximum unambiguous range of 150 km and unambiguous radial velocity of 8 m s^{-1}. The radar was run continuously in planned position indicator (PPI) mode, such that it completed a total of 12 full-circle scans from a minimum elevation angle of 0.5° up to 12.5°, taking approximately 5 min for each volume scan. All raw radar moments were visualized on site, transmitted out via cellular networks and displayed in real time on a public-facing website.

Several post-processing steps were needed to compute rainfall rates from the NOXP data, and these are summarized as a flowchart in Supplementary Fig. S2. The SCOP-ME algorithm (Kalogiros *et al.* 2014) was employed for several of these steps given its extensive use on X-band mobile radar data. These included the following steps: (1) ingest raw radar moments and correct for miscalibration, attenuation loss and partial beam blockages, and compute specific differential phase, K_{dp}; (2) compute rainfall rates from K_{dp} for elevation angles that were unobstructed by underlying terrain blockages; (3) aggregate instantaneous rainfall rates up to 15-min accumulations; (4) correct for true azimuthal pointing angle of the radar truck by comparing with the Multi-Radar Multi-Sensor (MRMS) radar products (Zhang *et al.* 2016), and (5) merge NOXP-based rainfall accumulations with MRMS.

Radar miscalibration, attenuation and partial beam blockages were likely to be present given the radar is often subject to vibration during transport, and the calibration is not carefully monitored like an operational radar. Further, the storms observed were convective thunderstorms with rain often mixed with hail, so attenuation was likely. Partial beam blockages were also potentially present owing to nearby trees, which were not considered during the beam blockage computations. The SCOP-ME algorithm was used to correct for all these issues using well-known procedures (i.e. self-consistency theory; Gorgucci *et al.* 1992), and it also computed K_{dp}, which is the derivative of the differential phase, φ_{dp}, with respect to range (Wang and Chandrasekar 2009). This variable is insensitive to miscalibration, attenuation loss (unless there is total signal loss) and partial beam blockage, and is thus the preferred variable to use for rainfall rate estimation.

The following X-band dual-polarization relation was used to compute rainfall rates:

$$R\,(K_{dp}) = 19.18K_{dp}^{0.85} \tag{1}$$

where R is in millimeters per hour (mm h^{-1}), and the specific differential phase, K_{dp}, is in degrees per kilometer (° km^{-1}). In order to avoid beam blockage, a dynamic selection approach was chosen, where the lowest elevation angle without blockage was chosen for each azimuth and range bin. Beam blockages by terrain, also referred to as occultation, were computed by comparing the radar beam heights with the underlying terrain. The height of the center of the radar beam was calculated as a function of range and elevation angle using a standard 4/3 Earth's radius assumption as in eqn (1.3) in Hong and Gourley (2015). These heights were then compared with a digital elevation model to yield a blockage map for each elevation angle. Specifically, the ASTER global digital elevation model version 2 with 1 arc s (~30 m) resolution was used (NASA/METI/AIST/Japan Spacesystems and US/Japan ASTER Science Team 2009). By using the terrain information and a three-dimensional model of the radar beam, beam blockages were estimated. This information was used to exclude highly occluded areas (>50% blockage) from further processing. Rainfall rates were then computed for K_{dp} values using Eqn 1 for the 1.8°, 3.1° and 4.0° elevation angles at the azimuth angles that were found to be less impacted by underlying terrain, and these data were used thereafter for rainfall estimation.

After calculating the NOXP rainfall rates, they were aggregated to 15-min accumulations. This was accomplished by considering all radar data collected within the 15-min window. In many cases, the 5–6 min spent for the radar to collect a volume of data (volume scan) would overlap the start/end times of the accumulation period. If this occurred, then the rainfall rate for that volume scan was applied to the specific time interval of data collection within the 15-min window. For instance, if a rainfall rate of 30 mm h^{-1} was computed from a volume scan that ended at 00:02, then it would be accumulated as (0.5 mm min^{-1} × 2 min = 1 mm), which would then be added to the rainfall collected after 00:03, and so on. Shorter accumulation intervals could have been considered, but the 15-min period corresponded to the shortest-duration accumulation period for the rain gauges. Accumulations over 15 min from the rain gauges were collected and transmitted, rather than the individual tips.

The remaining correction steps required the introduction of independent NEXRAD radar data from the operational MRMS algorithm to guide additional NOXP correction procedures (Zhang *et al.* 2016; Gourley 2024). MRMS uses a mosaic of radar data from adjacent NEXRAD and gap-filling radars to arrive at a synthetic, dual-polarization quantitative precipitation estimate (Zhang *et al.* 2020). In the case of Spring Creek, MRMS primarily used data from the KPUB WSR-88D radar located in Pueblo, CO, at a range of

140–155 km from the closest and furthest extents of the gaged basins. This placed the center of the lowest elevation angle at median heights of 1.6, 2.4 and 2.2 km AGL for Indian Creek, Middle Creek and Big Branch Creek basins, respectively. Despite this quite good coverage at low altitudes, the 150-km range of the nearest WSR-88D radar resulted in a 1.0° beamwidth that is approximately 2.4 km wide, which is undesirably coarse for the intended application. The radar's beamwidth is limited by the antenna size, and narrower data bins can only be realized at closer ranges to the radar. The MRMS algorithm uses nearest-neighbor resampling of the radar data to a 1-km^2 Cartesian grid to minimize information loss at closer ranges (Zhang *et al.* 2016).

There was uncertainty in the reported heading of the truck's pointing angle (yaw), although onboard hydraulic levelers were used to correct the pitch and roll of the vehicle. The vehicle was equipped with a magnetometer to report the vehicle's magnetic heading. Once the magnetic heading was reported, a correction for true north was calculated based on the vehicle's location. The instrument was known to be impacted by interference from sources that generate electromagnetic fields, such as a radar. As such, for each scan listed in Supplementary Table S1, MRMS hourly rainfall accumulations were used to diagnose NOXP pointing angle errors resulting in azimuthal offsets. This was accomplished by iteratively rotating the NOXP data in the azimuthal direction by 1° and computing the Pearson correlation coefficient with the MRMS rainfall fields. This approach ensured that the data were properly aligned, under the assumption that the alignment of the WSR-88D data represented a true north heading. In the first case, the correlation was maximized at a yaw angle offset of −16° (Supplementary Table S1). The vehicle was moved to a slightly different location within the park between cases in 2019 to minimize nearby tree blockages, and a new offset of −14° was calculated and applied. When NOXP radar returned to the field in 2021, another new offset of +2° was calculated for correct alignment using the same MRMS-guided approach (Supplementary Table S1).

NOXP radar's first observing period revealed a case of severe attenuation of the radar signal causing total loss as well as wedge-shaped artifacts of beam blockages caused by nearby trees. The NOXP rainfall field computed from K_{dp} showed obvious signs of blockage, resulting in wedge-shaped artifacts of lower or missing rainfall values. This confirmed the suspicion of trees yielding additional blockages beyond those computed from beam occultation calculations. This observing period is studied in more detail in the Results section, but the data required an additional step for creating the final rainfall product. Given the severe attenuation caused by a storm collocated with the radar, there were echoes observed on the burn area in the MRMS product that were completely unobserved by the NOXP radar. For this reason, we developed a data integration method that computed the average NOXP 15-min accumulation within each 1-km^2 MRMS grid cell. Given the 75-m resolution of the NOXP data, this resulted in approximately 177 grid cells within each MRMS grid cell. A bias was computed between the average NOXP rainfall accumulation and the MRMS value at each grid cell in the domain. This spatially varying bias was then applied back to the NOXP field so that it was consistent with MRMS, but still resolved spatial variability at scales smaller than 1 km. Furthermore, to address the situation of total loss of the NOXP signal, if the NOXP values were either less than 1 mm in 15 min or missing, then they were assigned the MRMS value. This product is referred to hereafter as the merged MRMS-NOXP product.

Case descriptions

All instruments were warm season deployments, such that they were only operated and maintained from approximately early May through to the end of September. In the intermountain West of the US, convective thunderstorms during this time of year are the primary sources of rainfall typically responsible for post-fire flash flood and debris flow initiation. Three cases were selected for detailed study based on data availability from the observatory and case magnitude (Table 2). There were several data outages

Table 2. Case descriptions.

Case number	Rain start (UTC)	Rain end (UTC)	Case end (UTC)	Max 15-min rain accumulation at USGS rain gauges (mm) (Hempel *et al.* 2025)	Local storm report (Iowa State University 2025)
1	2019-07-22 23:15	2019-07-23 02:45	2019-07-23 06:00	23.2 (Middle Creek) 9.8 (Indian Creek)	Flash flooding
2	2019-08-02 22:15	2019-08-03 02:00	2019-08-03 06:00	9.9 (Middle Creek) 7.1 (Indian Creek)	–
3	2021-07-31 22:45	2021-08-01 03:00	2021-08-01 06:00	26.8 (Middle Creek) 9.8 (Big Branch Creek)	Flash flooding, debris flow

due to sensors being moved throughout the experiment, data transmission or power problems and biological interferences. At Middle Creek, stage and velocity data were lost for 14 h during Case no. 1 owing to insufficient power. A larger solar panel was ordered and installed a couple weeks later to fix the issue. In 2021, a technician visited the Big Branch site and discovered the rain gauge cover was full of water because the screen was blocked by bees (see Supplementary Fig. S3). This caused rainfall data to be lost from 31 July to 5 August 2021, which included Case no. 3. Furthermore, the COVID-19 pandemic impacted operations at the NOXP radar site, limiting its deployment to the summers of 2019 and 2021. Table 1 provides a summary of the NOAA-USGS joint data collection effort on the Spring Creek burn area. Several of the figures from the mobile radar were made using the Py-ART open-source software (Helmus and Collis 2016). Additional plots and geospatial analyses were made possible using the Free and Open Source QGIS software (QGIS Development Team 2024).

Results

Evolution of a storm and its NOXP radar signatures: a detailed example from the 22 July 2019 case (Case no. 1)

Some of the insights gained and challenges encountered in this mobile radar deployment presented themselves on the first day of NOXP operations on 22 July 2019. A storm formed on the northern periphery of the burn area and was moving south at ~00:11 UTC (Coordinated Universal Time) on 23 July as seen in the NOXP reflectivity (Z_h) (Fig. 3*a*). Reflectivity represents the amount of energy that was backscattered to the radar by hydrometeors (i.e. raindrops). It is useful for revealing a storm's structure and is related to precipitation intensity. Fig. 3*a* shows a constant altitude planned position indicator (CAPPI) of Z_h, which is essentially a horizontal cross section through the 3D volume of data at an altitude of 2 km above the radar's elevation. This altitude for the CAPPI was chosen as a balance between revealing details at low levels and being just high enough

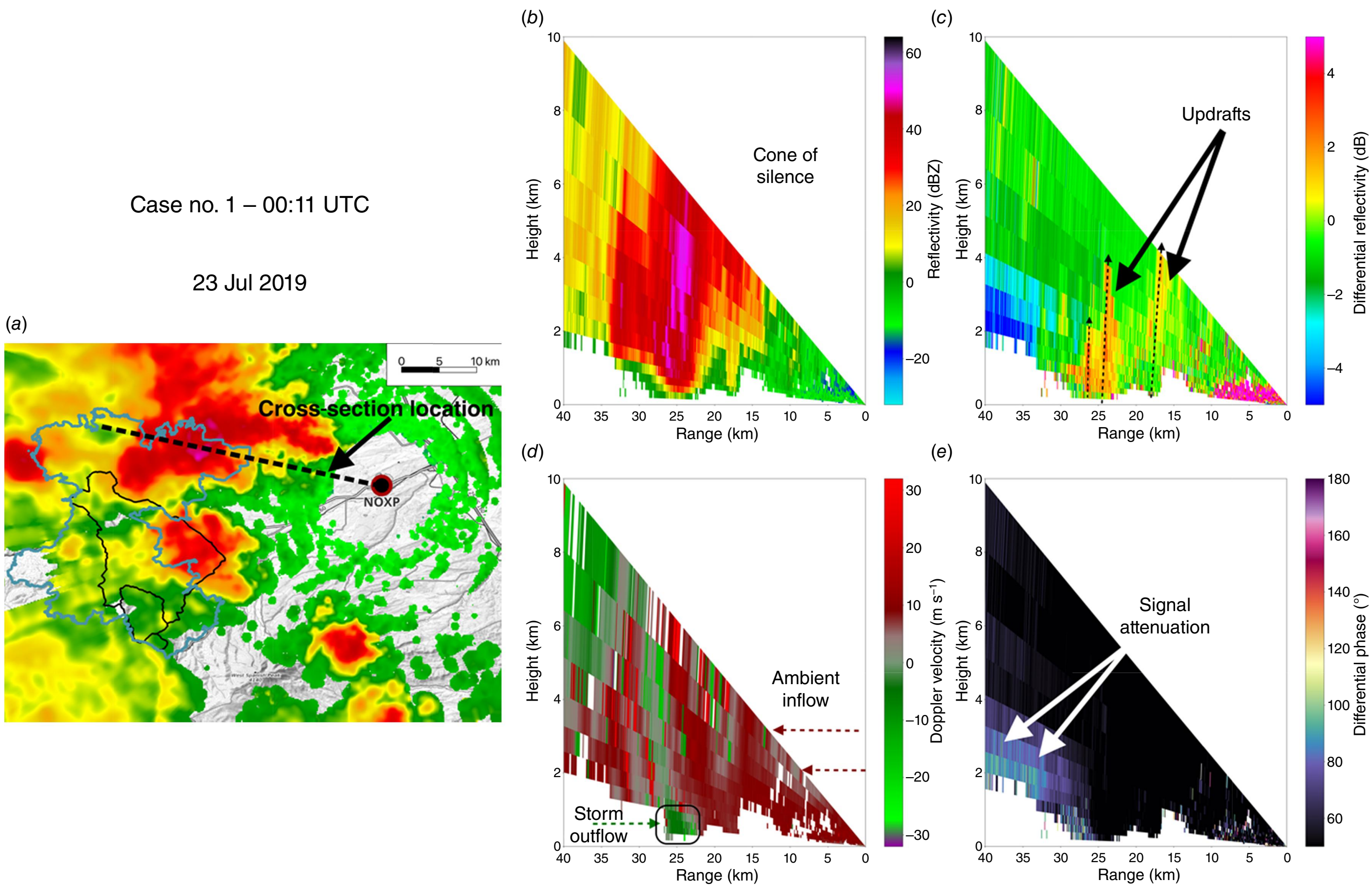

Fig. 3. Constant altitude planned position indicator (2 km) of NOXP reflectivity (dBZ) at 00:11 UTC on 23 July 2019, Case no. 1 (*a*). The dashed black line corresponds to an azimuth angle of 282°. Cross-section of NOXP reflectivity (dBZ) (*b*), differential reflectivity (dB) (*c*), radial velocity (m s^{-1}) (*d*), and differential phase (°) (*e*) at azimuth angle of 282°. Solid arrows highlight features discussed in text while dotted arrows correspond to airflows.

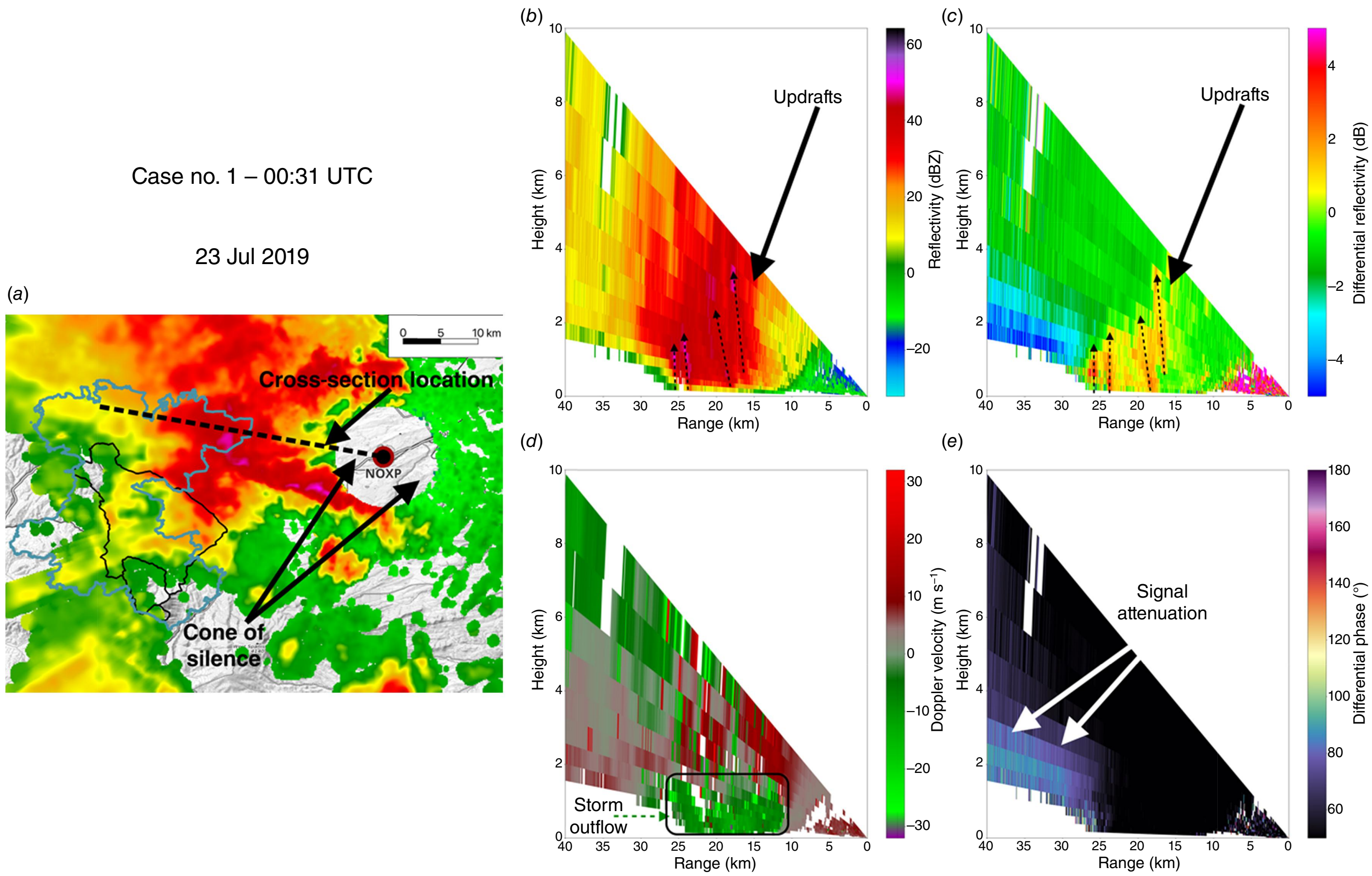

Fig. 4. Constant altitude planned position indicator (2 km) of NOXP reflectivity (dBZ) at 00:31 UTC on 23 July 2019, Case no. 1 (*a*). The dashed line corresponds to an azimuth angle of 280°. Cross-section of NOXP reflectivity (dBZ) (*b*), differential reflectivity (dB) (*c*), radial velocity (m s^{-1}) (*d*), and differential phase (°) (*e*) at azimuth angle of 280°. Solid arrows highlight features discussed in text while dotted arrows correspond to airflows.

above the surrounding terrain. The dashed line corresponds to an azimuth angle of 282° and was positioned through the center of the convection. Vertical cross-sections at this azimuth angle were reconstructed from the 3D volume of data. Fig. 3*b* shows the vertical extent of the storm, as revealed by the Z_h variable, exceeded the maximum altitude at which data were collected by the radar, into the radar's 'cone of silence'. At altitudes from the surface to 4 km, the differential reflectivity (Z_{dr}) variable showed relative maxima on the leading edges of the storm (Fig. 3*c*). This variable is computed from the ratio of reflectivity measured at horizontal and vertical polarization. Raindrops become oblate (horizontal dimension greater than vertical one) when they are falling owing to aerodynamic forces, causing them to flatten at the bottom and resemble a frisbee-like shape rather than a teardrop. Owing to these shapes, there will be more backscattered energy at horizontal polarization rather than at vertical, whereas if the hydrometeors were perfectly spherical, then the reflectivities at both polarizations would be the same and the ratio, or Z_{dr}, would be 1.0 (or 0 in decibels). The enhanced regions of Z_{dr} values oriented in columns have been associated with the presence of large drop growth and thus updrafts in deep, moist convective storms (Kumjian *et al.* 2014). Strong updrafts can initiate ice microphysical processes leading to the formation of hail. These inferred updrafts are annotated on Fig. 3*c*. The radial velocities shown in Fig. 3*d* indicated ambient (environmental) winds blowing east to west away from the radar and towards the storm, while at the lowest 1 km, there were inbound westerly winds associated with developing outflow from a downdraft. At ranges beyond 25 km, Fig. 3*e* shows values of φ_{dp} as high as 100°. The differential phase is a path-integrated variable, which is the difference in phase between the horizontally and vertically polarized signals. These differences in phase arise from the slightly longer time it takes for the horizontally polarized radar beam to propagate through raindrops compared with the vertically polarized beam. Like the Z_{dr} variable, these differences arise because of the increasing oblateness of the raindrops as they grow. Areas of increasing φ_{dp} are thus related to rainfall rates along the path. They are also related to the degree of signal attenuation (loss) in both Z_h and Z_{dr} behind the core of the

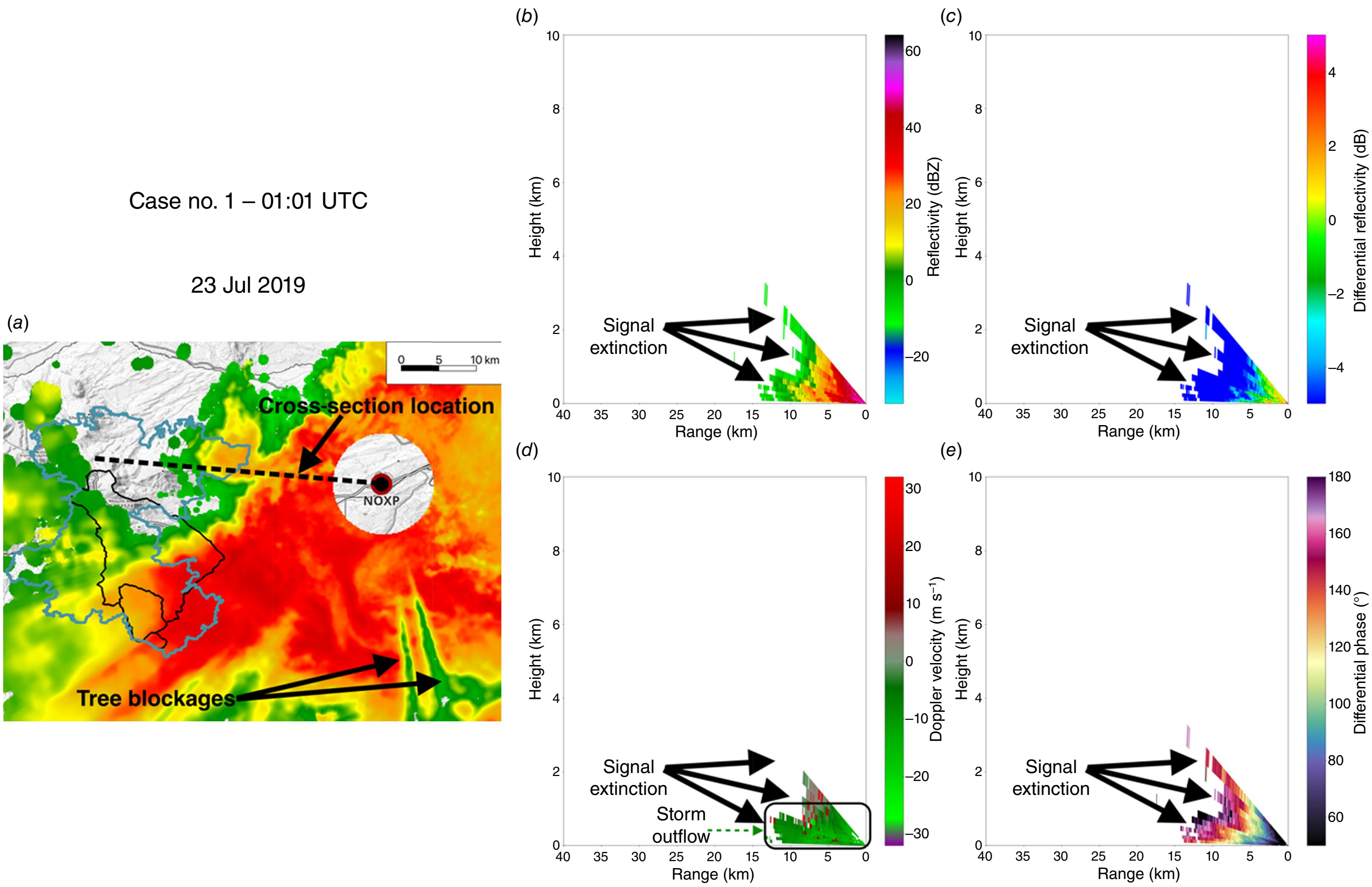

Fig. 5. Constant altitude planned position indicator (2 km) of NOXP reflectivity (dBZ) at 01:01 UTC on 23 July 2019, Case no. 1 (*a*). The dashed line corresponds to an azimuth angle of 275°. Cross section of NOXP reflectivity (dBZ) (*b*), differential reflectivity (dB) (*c*), radial velocity (m s^{-1}) (*d*), and differential phase (°) (*e*) at azimuth angle of 275°. Solid arrows highlight features discussed in text while dotted arrows correspond to airflows.

thunderstorm, resulting in undesirable negative values of Z_{dr} and decreases in Z_h.

Another 2-km CAPPI of Z_h was examined 20 min later (00:31 UTC) as the storm continued to intensify and propagate to the east (Fig. 4*a*). Some of the echoes had just begun to enter the Middle Creek basin on the burn area (Fig. 2). At low levels, individual updraft pulses can be discerned through the collocation of four Z_{dr} columns with enhanced Z_h values (Fig. 4*b*, *c*). The updrafts reached greater heights, up to 4 km, on the leading edge of the storm and became shallower moving closer to the core. Fig. 4*d* shows that the outflow had deepened to approximately 1.5 km and had become more expansive as the inbound velocities with the outflow spread to the east toward the NOXP location. The vertical cross-section of φ_{dp} looks quite similar to the prior cross-section with values generally less than 100° (Fig. 4*e*).

At 01:01 UTC, Fig. 5*a* shows that the storms that were previously threatening the northern end of the burn area had dissipated. The CAPPI also shows a circle of no echoes right on top of the NOXP radar. This is an artifact of constructing a CAPPI that intersects the radar's cone of silence. At 01:00 UTC, the operator logged 'Getting high winds and heavy rain at site.' At 01:03 UTC, they recorded the following: 'Small hail at site. I am right in the middle of the worst storm around with >50 kts shown on inbounds coming this way.' (Gourley 2025). The vertical cross-sections in Fig. 5*b–e* reveal much different patterns than the prior times. The high values of Z_h and Z_{dr} that previously extended more than 20 km in range diminished rapidly to their minimum values in less than 10 km (Fig. 5*b*, *c*). The radial velocity cross-section still had strong inbound velocities approaching 25 m s^{-1} at the radar site (Fig. 5*d*). Fig. 5*e* shows that the values of φ_{dp} had rapidly increased to their maximum values of 180° within only 10 km. These large values were associated with attenuation of the radar signal in rain mixed with small hail. Furthermore, the rainfall retrievals from 00:00 to 00:15 UTC using the $R(K_{dp})$ algorithm applied to NOXP data and from MRMS reveal that the X-band radar signal had become extinct to the southwest of the radar across Middle Creek basin on the burn area (Fig. 6*a*, *b*). This is confirmed by the presence of light rainfall accumulations (<5 mm) according to the MRMS

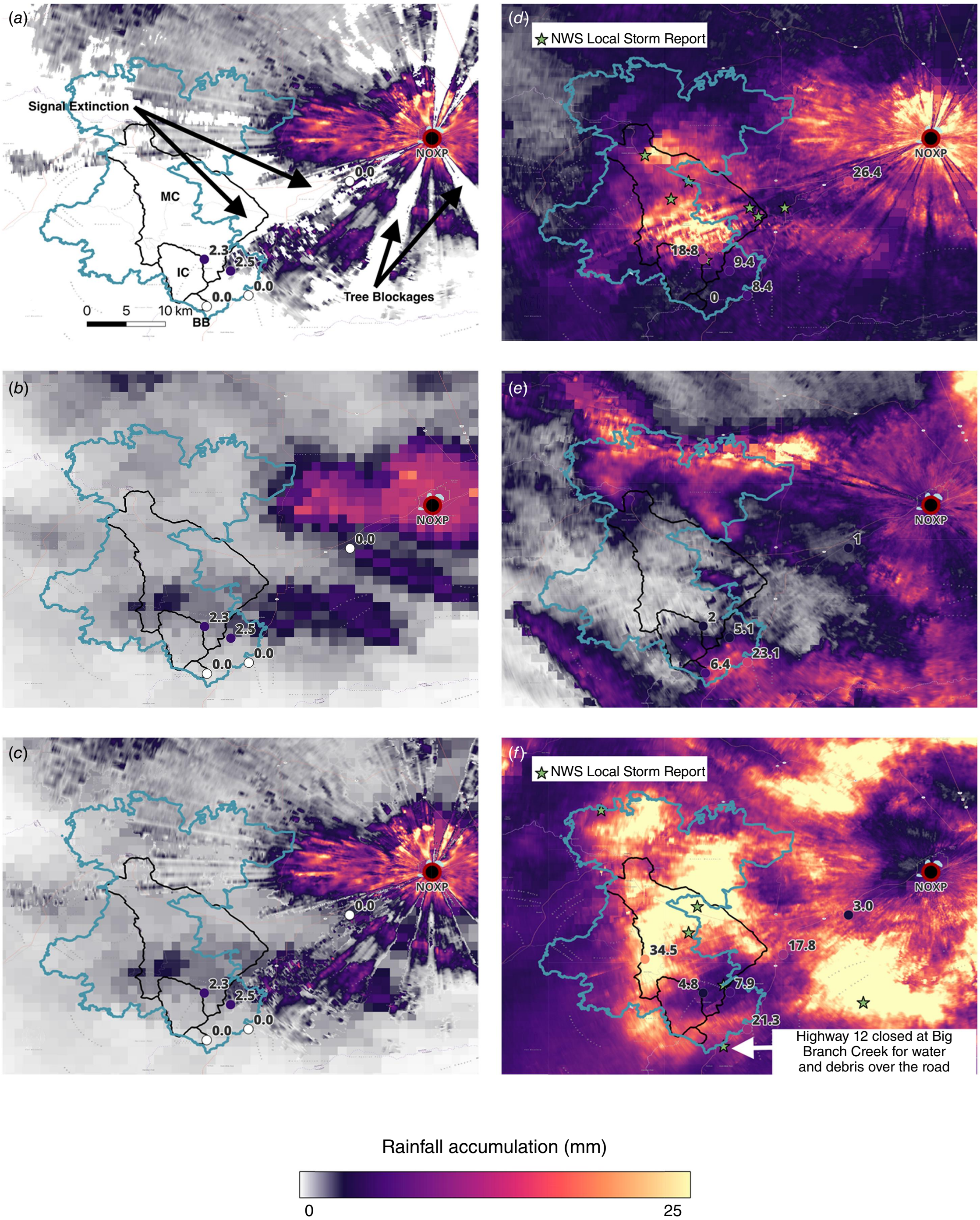

Fig. 6. Rainfall accumulated over 15 min ending at 01:15 UTC on 23 July 2019, Case no. 1, using $R(K_{dp})$ algorithm applied to NOXP data (*a*), MRMS radar-only product (*b*), and merged MRMS-NOXP product (*c*). Storm total rainfall using merged MRMS-NOXP product for Case no. 1 (*d*), Case no. 2 (*e*), and Case no. 3 (*f*). Rain gauge accumulations for the same time periods are shown as circles with black outlines and labeled in black text with a white outline (Hempel *et al.* 2025).

algorithm and by the USGS rain gauges. At 01:13 UTC, the radar operator noted the following: 'Looking at NEXRAD, my signal is horribly attenuated and can't see a storm on the S side of burn area. Only the storm right on top of me.' In summary, there were new storms forming in the gaged basins on the southern side of the burn area, but they appeared as 'missing data' from the perspective of the mobile radar (Fig. 6*a*, *b*).

Merged MRMS-NOXP products for all three cases

The challenges presented by Case no. 1 motivated the development of the merged rainfall estimation approach that is described in the Materials and Methods section. Additionally, the case analysis provides an opportunity to reveal radar-depicted characteristics such as strong updrafts, inflows and outflows, which provide a wealth of information beyond retrieving rainfall rates. Hereafter, the focus switches to the derived rainfall products for all three cases, flash flood reports and basin responses. Fig. 6*c* illustrates how the merged MRMS-NOXP product is capable of filling in gaps caused by substantial attenuation of the signal leading to extinction while maintaining the 75-m spatial resolution provided by the mobile radar in areas of optimal sampling. Furthermore, even without the signal extinction issue, the $R(K_{\mathrm{dp}})$ estimator can become biased in situations with rain mixed with small hail. Although their study was conducted using radar data at a different frequency (S band), Kumjian *et al.* (2019) examined storms in Colorado that produced substantial hail accumulation and found that K_{dp} can become biased anomalously highly in the presence of small, melting hail. This also causes large differential attenuation, which can be detected by large swaths of negative Z_{dr} values extending downrange from the hail core. This behavior was present in all the cross-sections of differential reflectivity shown in Figs 6*c*, 7*c* and 8*c*, thus supporting the extension of this finding to X-band radar studies. The $R(K_{\mathrm{dp}})$ bias was corrected through the incorporation of the MRMS rainfall estimator at 1-km pixel resolution (Fig. 6*a*–*c*).

The merged MRMS-NOXP product was generated for the three cases listed in Table 2. At each 15-min time step, the nearest 75-m pixel was paired with the collocated rain gauge. These values were then accumulated for the case duration to yield plots of storm total rainfall, shown in Fig. 6*d*–*f*. Overlain on this figure are storm total accumulations from rain gauges plotted in the same color scale as the merged product as well as the locations and narratives contained within Local Storm Reports (LSRs) of flash flooding recorded by the NWS office in Pueblo, CO (Iowa State University 2025).

The merged product highlights two regions that received up to 45 mm of storm total rainfall during Case no. 1: a swath centered on the radar site associated with the storm described in the previous section and a second maximum over Middle Creek basin (Fig. 6*d*). Most of the USGS rain gauges were situated on the southern end of the burn area (Fig. 2), and none of them captured the rainfall maximum in Middle Creek and northern Indian Creek basins (US Geological Survey 2020; Hempel *et al.* 2025). Nevertheless, there is agreement within 15% between the rain gauge accumulations and the merged product on the periphery of the heaviest rain that fell. The LSRs indicated multiple impacts from the rainfall with most of the reports occurring within or just downstream (west) of Middle Creek basin.

During Case no. 2, the rain gauge at Big Branch accumulated a storm total amount of 6.4 mm at the basin outlet whereas the gauge downstream (outside of the burn area) received 23.1 mm of rain (Fig. 6*e*). Owing to the lower rainfall intensities, there were no LSRs recorded with this case. Case no. 3 exhibited significant rainfall throughout the burn area with storm total accumulations up to 50 mm primarily concentrated over Middle Creek and Big Branch (Fig. 6*f*). The rain gauge at Big Branch was not usable during Case no. 3 owing to the clogging of the screen by bees (Supplementary Fig. S3). Also, similarly to Case no. 1,

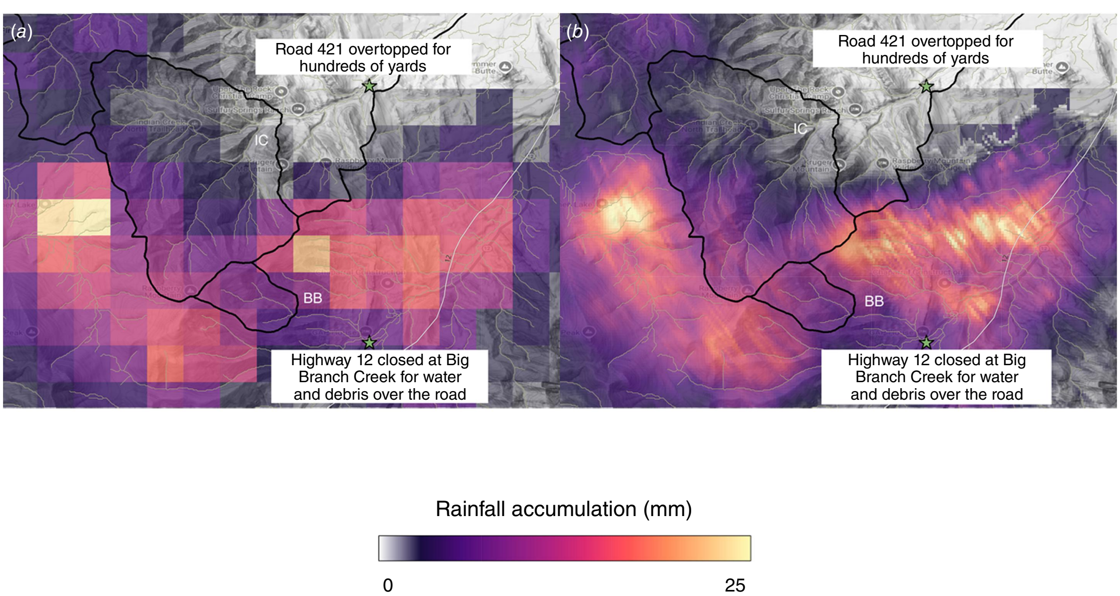

Fig. 7. Rainfall accumulated over 15 min (mm) ending at 23:00 UTC on 31 July 2021, Case no. 3, using MRMS (*a*), and the merged MRMS-NOXP product (*b*). Green stars represent the locations of NWS Local Storm Reports.

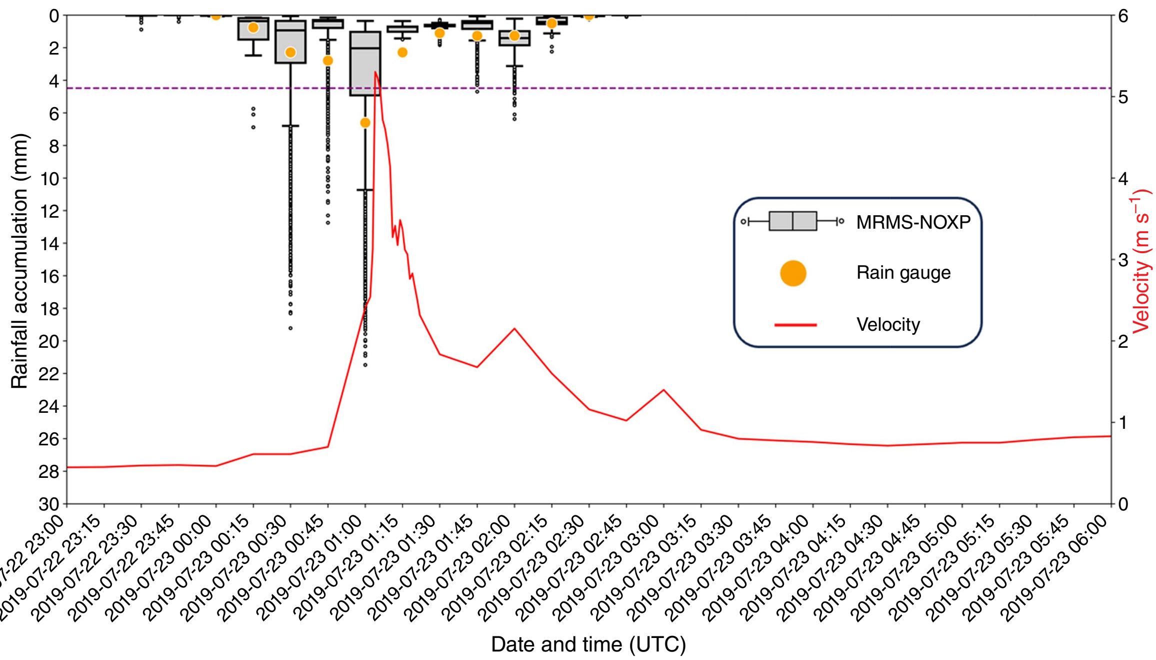

Fig. 8. Time series of the 15-min MRMS-NOXP merged rainfall product (inverted box-and-whisker plotted against primary y-axis), rain gauge accumulation at basin outlet, and flow velocity (on secondary y-axis) for Case no. 1 at Indian Creek station. The dashed purple line corresponds to the USGS debris flow threshold (USGS Post-Fire Debris Flow Hazard Assessment Viewer 2025).

there was a dearth of rain gauges in Middle Creek to evaluate the spatially distributed rainfall estimates from the merged product. However, the ASOS/AWOS station at La Veta Pass (KVTP) was available during this case and was incorporated in the evaluation. There is very good agreement in the storm total accumulations between the USGS rain gauges and the merged product, with a slight indication of overestimation at the KVTP rain gauge, which accumulated a total of 34.5 mm. Given the unknown quality of the rain gauge data for this station, this result is not conclusive of widespread overestimation throughout the burn area (i.e. Middle Creek and Big Branch). The LSRs were primarily concentrated in Middle Creek with several county roads that were overtopped by flood waters, but the most significant impact was the closure of State Highway 12 downstream from Big Branch owing to a debris flow covering the roadway. This cut off all traffic between the towns of Cuchara and La Veta, CO (Gourley 2025).

Despite rain gauges having their own sources of error due to wind, siting and biological interferences, as well as lacking the ability to resolve spatial patterns in convective rainfall, they were used to statistically evaluate the merged MRMS-NOXP product. Each of the 15-min accumulations from the rain gauges and the collocated pixels from the merged product were paired for all time steps of the three cases studied. Supplementary Fig. S4 shows the scatterplot of the 15-min accumulations from MRMS and the merged MRMS-NOXP product compared with the gauges. Overall, both products behaved very similarly, which is not surprising given that the MRMS product was used to bias-adjust the merged product on a pixel-by-pixel basis. The statistical comparison in the figure inset indicates slightly overestimated rainfall compared with the rain gauge accumulations from both products, but the performance according to all statistics (1) of both is similar, and (2) is indicative of accurate retrievals of rainfall rates by the radars.

Scale-dependent depictions of rainfall fields

The benefits of having a mobile weather radar for identifying storm microphysical and dynamical processes and accurately retrieving rainfall have been demonstrated. Although rain rates were natively produced on a 5–6 min basis following the completion of each volume scan, they were aggregated up to 15-min accumulations to compare with the rain gauge accumulations. Furthermore, Staley *et al.* (2017) developed logistic regression models for predicting the likelihood of postfire debris flow hazards based on SBS, slope, soil erodibility factor and precipitation intensity at 15-, 30- and 60-min durations, and the radar rainfall estimates are compared with these thresholds. The most beneficial use of the radar is the ability to provide spatial representations of rainfall fields at 1-km pixel resolution for MRMS and 75-m resolution for the merged MRMS-NOXP product. Case no. 1 had multiple reports of flash flooding in Middle Creek basin, but the causative rainfall was only captured by the MRMS and merged MRMS-NOXP products and was largely unobserved by the rain gauge network. Case no. 3 had similar deficiencies with rain gauge spatial coverage and representation (Fig. 6*f*).

A 15-min period ending at 23:00 UTC for Case no. 3 was chosen to illustrate aspects of scale-dependent depictions of rainfall fields from the perspectives of rain gauges, MRMS, and the merged MRMS-NOXP product. This was the time when Big Branch received the heaviest rainfall that resulted in the debris flow event that closed State Highway 12 downstream. The USGS rain gauges missed most of the causative rainfall including the Big Branch site because the rain gauge was inoperable due to the clogging issue. MRMS, however, captured the overall footprint of the rainfall (Fig. 7*a*). In comparison with the merged product, there were several scale differences due to pixel resolution (Fig. 7*b*). When focusing on Big Branch basin, MRMS only had a single pixel wholly contained in the basin, which indicated slightly heavier rainfall in the upper reaches of the basin. The merged product revealed much more detail with some pixels exceeding 13 mm in the upper reaches of the basin while MRMS showed 10.6 mm. Furthermore, the merged product resolved a gradient in the rainfall with a minimum of 6.5 mm at the Big Branch basin outlet where the USGS site was located (Fig. 7*b*). Even if the rain gauge had been functional, it represents a point location; and therefore, would likely not have been representative of the heavier rainfall that had fallen upstream on the potential debris flow initiation region.

Mobile radar provides insights into hydrologic responses

Insights into hydrologic responses to highly resolved rainfall fields on burn areas are provided with the stream radar data. The analysis plots the times series of the MRMS-NOXP rainfall with the basin response variables, stage and velocity. Further, we include the rain gauge data (if available) and include debris flow thresholds at 50% probability supplied by the USGS (USGS Post-Fire Debris Flow Hazard Assessment Viewer 2025). The larger basins (Middle Creek and Indian Creek) had sub-basin thresholds, and the average values are plotted as horizontal lines on the time series plots. The MRMS-NOXP rainfall product was averaged within each basin, so they can be compared with the basin response variables.

For Case no. 1, the heaviest rainfall and subsequent flash flood LSRs occurred in Middle Creek basin, but there were no specific debris flow events recorded. Unfortunately, the stage and velocity data were missing for this case owing to the power supply issue previously discussed. Fig. 8 shows the time series of the MRMS-NOXP merged rainfall product with the basin-wide distribution of rainfall represented by a box-and-whisker plot and the subsequent stream response represented by the observed surface velocity at Indian Creek. The 50, 75 and 90% rainfall quantiles peaked at 01:00 UTC, while the rain gauge at Indian Creek exceeded the USGS debris flow threshold at the same time. The stream radar measured a maximum surface velocity of 5.3 m s^{-1} at 01:04 UTC. This is believed to be the pulse that resulted in the single LSR stating a 'significant amount of water over the road coming from Indian Creek', but there was no report of a debris flow (Fig. 6*d*). Given the 24.7-km^2 area of the Indian Creek basin, it is unlikely that this peak in the velocity response corresponded to the rainfall occurring just 4 min prior but instead was likely a combined, dynamic response to the rainfall that occurred in the upper reaches beginning at 00:15 UTC and propagated downstream along with the runoff peak. This inference is supported by examination of the time series of MRMS-NOXP rainfall quantiles, which reached relative maxima three times at 00:30, 01:00 and 02:00 UTC that led to corresponding peaks in the velocity responses at 01:04, 02:00 and 03:00 UTC. Note that the time series of the rain gauge at the basin outlet only peaked twice.

Case no. 2 had no flash flood LSRs recorded, yet the case supplies meaningful information regarding rainfall runoff responses on burn areas. The time series of MRMS-NOXP merged rainfall quantiles in Fig. 9*a* for Middle Creek reached maximum values at 00:15 UTC on 3 Aug 2019. The responses in surface velocity (1.2 and 1.4 m s^{-1}) occurred at 03:15 and 05:00 UTC and represent an attenuated flood wave because of the rainfall being limited to the upper reaches of Middle Creek basin (Fig. 6*e*). The rainfall being concentrated in the upper reaches of Middle Creek with a large basin area of 175.3 km^2 resulted in a flood wave that lagged the rainfall by more than 3 h, and the peak values were attenuated as it propagated downstream. The prediction of flood waves and travel times using similar instruments was explored in more detail by Fulton *et al.* (2024). Additional evidence of the flood peak attenuation is supported by the data shown in Fig. 9*b* at the Indian Creek station. The rainfall peaked at 00:15 UTC, and this is the same rain that resulted in the Middle Creek runoff response, as the Indian Creek station is upstream from the Middle Creek station (Fig. 2). In this case, the stream radar measured a peak in the surface velocity of 2.5 m s^{-1} that lagged the causative rainfall by 30 min. The magnitude of the peak velocity decreased as the flood wave propagated downstream and reached the Middle Creek stream radar 2.5 h later (Fig. 9*a*). In comparing the time series plots at Indian Creek for Cases nos 1 and 2, the magnitude of the peaks in rainfall was very similar, but Case no. 1 had double the magnitude of peak velocity response and a recorded LSR (Fig. 8). The heaviest rainfall in Case no. 2 only occurred for a single 15-min time step whereas Case no. 1 experienced longer-duration rainfall. This points to more complex rainfall runoff behavior rather than a simple comparison of rainfall amounts with thresholds at a single time step. As with Case no. 1, the rain gauge values at the basin outlet at Indian Creek station generally fall within the distribution of

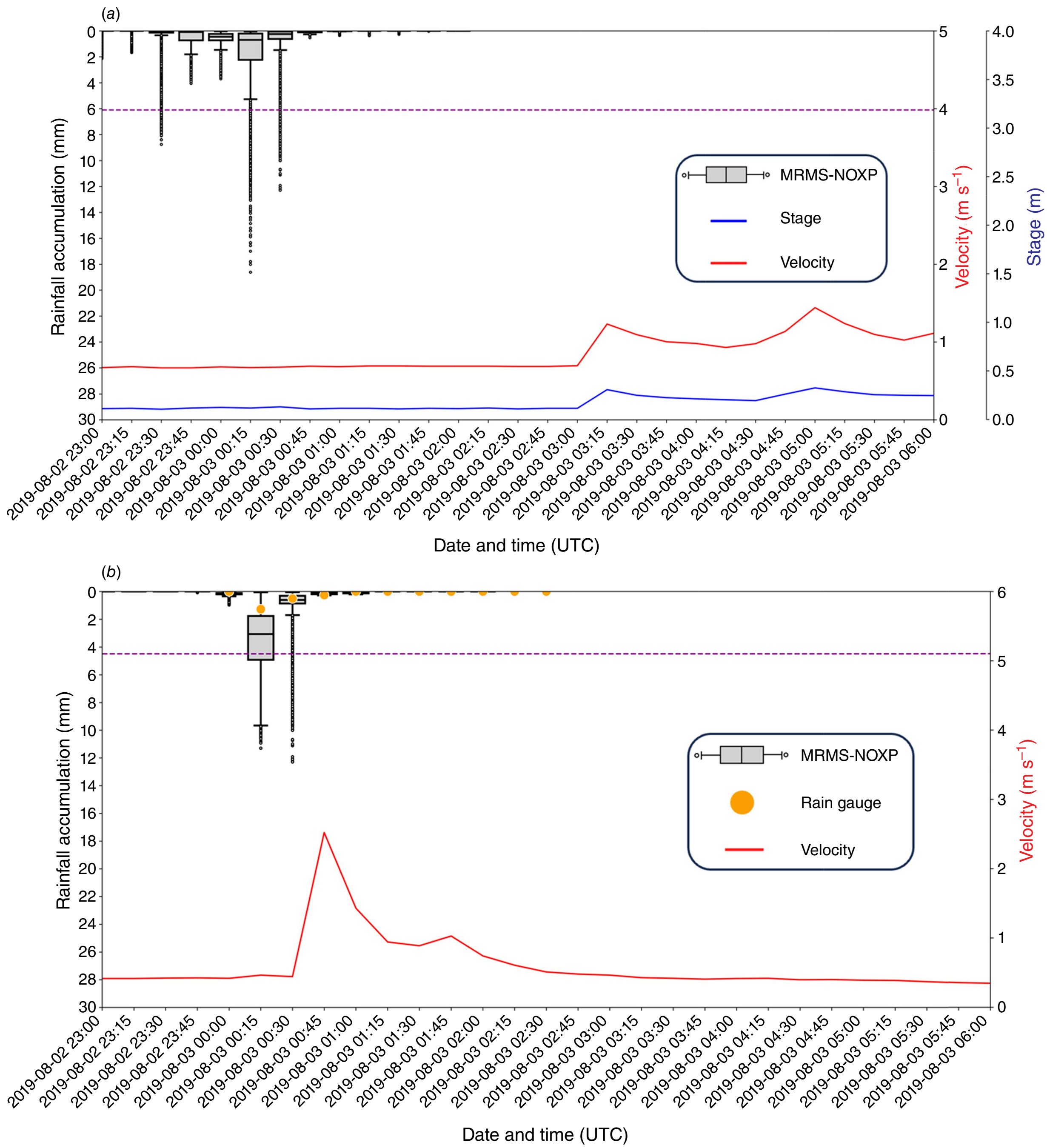

Fig. 9. Time series of the 15-min MRMS-NOXP merged rainfall product (inverted box-n-whisker plotted against primary *y*-axis), and flow velocity and stage (on secondary *y*-axis) for Case no. 2 at Middle Creek site (*a*), and Indian Creek site (*b*), which also shows rain gauge accumulations. The dashed purple line corresponds to the USGS debris flow threshold (USGS Post-Fire Debris Flow Hazard Assessment Viewer 2025).

rainfall as represented by the box-and-whisker plots of the MRMS-NOXP product.

Case no. 3 had the most extreme and widespread rainfall that impacted all three gaged basins (Fig. 6*f*), with the most substantial being the debris flow event from Big Branch. The Indian Creek stream radar had been decommissioned after 2020 and was not available for this case. Three LSRs were recorded within Middle Creek, citing minor roads being covered by water but no debris flows. The time series plot in Fig. 10*a* shows the upper quartiles of 15-min rainfall accumulations that ended at 23:15 UTC on 31 July 2021 exceeded the USGS debris flow threshold at Middle Creek. This resulted in an initial peak in stream velocity of 4.4 m s^{-1} that occurred at 01:00 UTC, lagging the causative

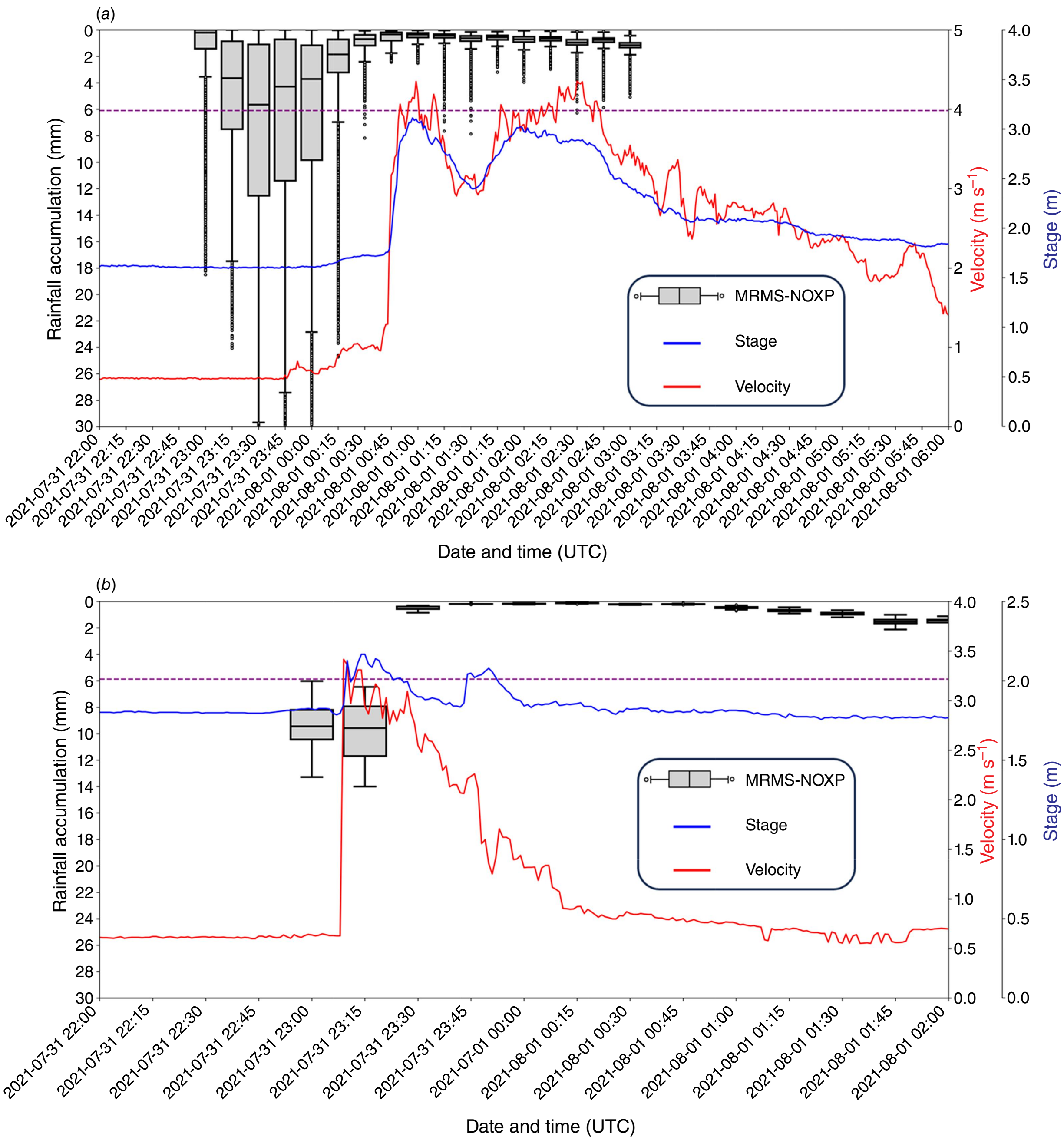

Fig. 10. Time series of the 15-min MRMS-NOXP merged rainfall product (inverted box-and-whisker plotted against primary *y*-axis), and flow velocity and stage (on secondary *y*-axis) for Case no. 3 at Middle Creek site (*a*), and Big Branch site (*b*). The dashed purple line corresponds to the USGS debris flow threshold (USGS Post-Fire Debris Flow Hazard Assessment Viewer 2025).

rainfall by 1.75 h. A second peak in velocity of the same magnitude occurred at 02:30 UTC (Fig. 10*a*) that was not clearly associated with a peak in rainfall and highlights the complexity of runoff behavior to sub-basin-scale rainfall variability. This issue becomes more pertinent with increasing basin size owing to the addition of flow pathways that can converge at a single point at the stream radar location.

The most substantial case measured by the experimental observatory deployment occurred downstream from the Big Branch site during Case no. 3 with the closure of State Highway 12 because of debris and floodwater covering the highway. Fig. 10*b* shows the time series of the MRMS-NOXP merged rainfall product, stage and surface velocity. At 23:00 UTC on 31 July 2021, the median of the basin rainfall distribution reached 9.4 mm in 15 min (Fig. 10*b*) with a maximum of 13.5 mm concentrated in the basin headwaters and 6.1 mm at the outlet (Fig. 7*b*). At 23:09 UTC, *only 9 min later*, the surface velocity jumped from an initial value of 0.6 to 3.4 m s^{-1} in just 1 min. The stream stage, however, responded at the same time as the surface velocity but not nearly with the same magnitude. The cross-sectional wetted area may have increased, which points to the need for bathymetry measurements in small streams, especially those that are prone to rapid geomorphological changes such as on burn areas. The increased sensitivity of velocity response compared with stage is a finding supported by other studies using stream stage and velocity observations (i.e. Gourley 2017; Fulton *et al.* 2024). Images from the trail camera at Big Branch are shown in Supplementary Fig. S5 at 22:53 and 23:13 UTC, just before and during the extreme runoff response. In addition to providing security and situational awareness of the stations, the camera reveals the high velocity flows that resulted from the precipitation that was concentrated in the basin headwaters. The average slope of the basin that generated high-velocity discharge is approximately 24°, with a maximum of 41°. There were individual pieces of woody debris (limbs) that were transported downstream by the time the next image was captured in Supplementary Fig. S5.

Discussion

The concurrence of wildfire impacts and complex terrain poses substantial challenges to conventional observing systems that were designed for the observation of rainfall and hydrologic responses across the US. These observing systems include the NEXRAD radar network, rain gauge networks and the USGS streamgage network, each of which has coverage shortcomings in the western US. The coverage problem is exacerbated by the abrupt vulnerability of the landscape to flash flooding, severe erosion and debris flows. These extreme hydrologic responses and associated downstream impacts can be initiated by rather unexceptional rainfall rates. As an example, the debris flow threshold at the Big Branch station for a 15-min duration rainfall was 5.9 mm (USGS Post-Fire Debris Flow Hazard Assessment Viewer 2025). The associated 1-year average recurrence interval rainfall accumulation for the same duration at that location is 11.3 mm, or approximately double the debris flow threshold. Given the high likelihood for extreme hydrologic responses following wildfire, the need to monitor the causative rainfall becomes paramount.

This study examined rainfall fields as represented by an experimental, well-calibrated rain gauge network, MRMS (which uses NEXRAD data) and an X-band mobile weather radar. Rain gauges have a long history of applications for rainfall studies given their generally high accuracy at a point and simplicity to deploy, calibrate and maintain. The cases analyzed in this study showed situations where rainfall maxima and intra-basin gradients occurred in locations that were not sampled by the rain gauge network. In Case no. 3, these rainfall amounts were substantial in that they were concentrated upstream in potential debris flow initiation regions, and there were observed reports of road impacts from flash flooding and debris flows downstream. Furthermore, the rain gauges were shown to have their own issues with reliability, including loss of power and biological interferences. Although the gauges were shown to have value for evaluating and calibrating remotely sensed rainfall amounts, this study suggests that they need not be the sole source of information used to monitor and forecast rainfall-triggered flash flooding, severe erosion and debris flows on burn areas. Radar also offers the capability to monitor storms in regions surrounding and upstream of a burn area, provided there are no substantial beam blockages by the terrain. If there are, then mobile radars can be employed to fill these voids. These instruments can be useful for providing several minutes of warning lead time as a first line of defense for potentially impending extreme hydrologic responses.

Radar-based rainfall estimates do not come error-free, however. Issues with radar quantitative precipitation estimates (QPEs) are well known and tend to be amplified in complex terrain (Germann *et al.* 2006). There are some new, machine learning-based approaches that show promise in the western US (i.e. Osborne *et al.* 2023), but it is unlikely that these QPEs could satisfy the high temporal and spatial resolution requirement on burn areas. Despite the Pueblo WSR-88D radar being 150 km away from the Spring Creek burn area, the sloping terrain enabled coverage within 2.4 km AGL (Fig. 1). The penalty for the long range to the radar meant the pixels were 2.4 km wide. Case no. 3 revealed that the 1-km pixel resolution rainfall with MRMS (which was oversampling the native 2.4-km radar pixels) was insufficient for resolving the detailed rainfall patterns in Big Branch basin, especially as compared with the 75-m QPE from the merged MRMS-NOXP product; this was a rather fortuitous setting for NEXRAD considering the reasonable low-level coverage provided given the sloping terrain, which counteracts earth curvature effects. There are vast areas in the western US that remain poorly sampled at low levels by the NEXRAD network (Fig. 1).

For post-fire monitoring, mobile weather radars can provide extended coverage in regions outside a burn area, giving lead time for approaching storms and resolve rainfall patterns and gradients at pixel resolutions generally less than 100 m. The 75-m pixel resolution with rainfall resolved by the mobile radar can identify situations where there is heavy rainfall occurring in a potential debris flow source area. This could be a major influence on debris flow initiation, which is not adequately captured at resolutions associated with NEXRAD. Use of mobile radar data can introduce an assortment of additional issues. Case no. 1 exposed a situation where attenuation caused by heavy rain mixed with small hail caused signal extinction and loss of data over the burn area. Even without the attenuation and signal loss issues, QPE algorithms at X band are still in development. The siting of the mobile radar requires good visibility over the burn area without intervening blockages by terrain or trees. Trees in close proximity to NOXP at Lathrop State Park caused blockage-based spokes and other wedge-shaped artifacts in the QPE fields, requiring a merging with the MRMS product. There was no access to commercial power, requiring the use of a generator and on-site operation by trained personnel. There was one case in 2021 (not shown) where storms started earlier than expected when the radar operator was not at the radar site, and the case was missed.

Mobile weather radars offer the potential to fill gaps in the operational NEXRAD radar network, which are plentiful in mountainous areas. In this study, the NEXRAD-based MRMS rainfall estimates were needed to calibrate the azimuth angle of the mobile radar data and to provide bias adjustment of the derived rainfall rates. To maximize the application of a mobile radar as a true gap filler, it would need to provide accurate estimates of rainfall without the reliance of co-located MRMS data. Several considerations, listed below, would need to be addressed to achieve this goal. First, an alternative to a magnetometer needs to be implemented to report the vehicle's magnetic heading. The performance of next-generation mobile radars for rainfall monitoring in burn areas may be improved by operating at C-band frequencies rather than X band. The primary benefit is less attenuation in rain and subsequent signal loss. The downsides for a C-band mobile radar systems are higher costs associated with the transmitter and a larger beamwidth (and coarser spatial resolution) for the same diameter of the parabolic dish as X band. The relatively larger beamwidth with a C-band radar can be compensated by siting the radar closer to the burn area. Furthermore, the use of a radome can reduce attenuation caused by a wet antenna and provide additional protection during hail and high winds. Deliberate siting can minimize blockages by trees. This can be further mitigated by equipping the radar with a hydraulic lift system that will raise the antenna higher above the cab of the vehicle. If there is access to commercial power, then the mobile radars may be capable of operating remotely so as to avoid data loss during unanticipated precipitation events, a situation not uncommon in complex terrain. The data flows may be improved by enabling real-time transmission via multiple options including cellular, wifi and satellite. These data may then be readily visualized for access by project partners and integrated into the operational MRMS software. The merging technique of NOXP and MRMS offers a simple, proof-of-concept technique that was performed during a post-processing step. An improved, alternative approach for consideration may be to mosaic the mobile radar variables with NEXRAD and computation of rainfall rates in real-time, a capability that is currently being demonstrated within the MRMS system (e.g. NOAA Multi-Radar/Multi-Sensor System (MRMS) 2024).

Conventional streamgages are rarely situated on streams that have experienced wildfire and are in locations vulnerable to flash flooding and debris flows. Additional observations of hydrologic response are needed on burn areas, similarly to the need for mobile weather radars. Given the high likelihood of there being a rainfall-triggered flash flood or debris flow event during the first year following the fire, non-contact instruments to measure hydrologic responses are preferred (Kean *et al.* 2011; Ebel *et al.* 2012; Rengers *et al.* 2016). They are less vulnerable to being lost during floods as compared with instruments that are in contact with the water (e.g. pressure transducers) and they utilize advanced data logging, which enables real-time alerting (via SMS) to local partners as well as increasing the frequency of observations (up to 1 min in this study) once user-defined alert thresholds have been exceeded.

The next-generation experimental observatory may benefit from beginning with coordination and prioritization among the federal, state and local agencies involved. The observatory may consider the observational assets and characteristics provided in this section; there is additional uncrewed aerial system (UAS)-based instrumentation that can contribute to the observation of debris flows including runout area, volume and mass, as well as vegetation health and recovery. Lastly, given the potential significance and likelihood of flash flooding and debris flow impacts on communities, the experimental observatory may benefit from emphasizing real-time data access, visualization, integration into decision support systems and alerting capabilities to the local authorities.

Conclusions

This study demonstrated the utility of the post-fire hydrometeorological observatory for supplying data to reveal unique insights on spatiotemporal rainfall patterns and their hydrologic responses on wildfire-impacted landscapes as well as providing real-time early alerting features to local partners, government agencies and local municipalities. The findings from this study are summarized as follows:

- The greatest benefit of the mobile radar was providing accurate rainfall estimates at 75-m pixel resolution, which revealed heavy rainfall occurring in a potential debris-flow source area.
- Rain gauge data were shown to be useful for assessing the accuracy of the mobile radar rainfall estimates, yet they lacked the spatial density needed for adequate post-fire monitoring.
- The combination of the mobile radar data with the non-contact stream radars provided unique insights into rainfall runoff behaviors with the added benefit of real-time

data transmission, alerting and visualization for local authorities.

Additional work evaluating the suggestions provided in the Discussion section could advance and improve the observational capabilities of the post-fire hydrometeorological observatory for burn area deployments. The next-generation observatory, supplemented by new mobile radars, could be implemented on current and additional burn areas to gain further insights into rainfall runoff patterns and to inform real-time decision support for potentially vulnerable downstream communities.

Supplementary material

Supplementary material is available online.

References

Abatzoglou JT, Williams AP (2006) Impact of anthropogenic climate change on wildfire across western US forests. *Proceedings of the National Academy of Sciences* **113**, 11770–11775. doi:10.1073/pnas.1607171113

Alter JC (1937) Shielded storage precipitation gages. *Monthly Weather Review* **65**, 262–265. doi:10.1175/1520-0493(1937)65 < 262:SSPG > 2.0.CO;2

Colorado Encyclopedia (2020) Spring Creek Fire. Available at https://coloradoencyclopedia.org/article/spring-creek-fire [accessed 24 September 2024]

Dennison PE, Brewer SC, Arnold JD, Moritz MA (2014) Large wildfire trends in the western United States, 1984–2011. *Geophysical Research Letters* **41**, 2928–2933. doi:10.1002/2014GL059576

Ebel BA, Moody JA, Martin DA (2012) Hydrologic conditions controlling runoff generation immediately after wildfire. *Water Resources Research* **48**, W03529. doi:10.1029/2011WR011470

Eberts SM, Woodside MD, Landers MN, Wagner CR (2018) Monitoring the pulse of our Nation's rivers and streams—The US Geological Survey streamgaging network, Fact Sheet 2018–3081, 2 p. (US Geological Survey) doi:10.3133/fs20183081

Fulton J, Hall N, Hempel L, Gourley JJ, Henneberg M, Kohn M, Famer W, Asquith W, Wasielewski D, Stecklein A, Mommandi A, Khan A (2024) Use of Doppler velocity radars to monitor and predict debris and flood wave velocities and travel times in post-wildfire basins. *Journal of Hydrology X* **24**, 100180. doi:10.1016/j.hydroa.2024.100180

Germann U, Galli G, Boscacci M, Bolliger M (2006) Radar precipitation measurement in a mountainous region. *Quarterly Journal of the Royal Meteorological Society* **132**, 1669–1692. doi:10.1256/qj.05.190

Gorgucci E, Scarchilli G, Chandrasekar V (1992) Calibration of radars using polarimetric techniques. *IEEE Transactions on Geoscience and Remote Sensing* **30**, 853–858. doi:10.1109/36.175319

Gourley JJ (2017) In pursuit of flash flood data. *Eos* **98**, doi:10.1029/2018EO079723

Gourley J (2024) 'Mobile radar data for 3 cases [Dataset].' (Zenodo). doi:10.5281/zenodo.13334194

Gourley J (2025) 'NOXP operator logs for 3 cases collected near Spring Creek burn area.' (Zenodo). doi:10.5281/zenodo.14630315.

Habib E, Krajewski WF, Ciach GJ (2001) Estimation of rainfall interstation correlation. *Journal of Hydrometeorology* **2**, 621–629. doi:10.1175/1525-7541(2001)002 < 0621:EORIC > 2.0.CO;2

Helmus JJ, Collis SM (2016) The Python ARM Radar Toolkit (Py-ART), a library for working with weather radar data in the Python programming language. *Journal of Open Research Software* **4**(1), e25. doi:10.5334/jors.119

Hempel LA, Fulton JW, Gourley JJ, Mcdermott WR, Kohn MS, Bock AR, Henneberg MF (2025) Precipitation, river surface velocity, and river stage measurements within the Spring Creek Burn Scar, Colorado, USA, during select storms in 2019 and 2021. (US Geological Survey). doi:10.5066/P133XUDC

Highway of Legends (2024) Colorado Department of Transportation. Available at https://www.codot.gov/travel/colorado-byways/southeast/highway-legends [accessed 10 January 2025].

Hong Y, Gourley JJ (2015) 'Radar Hydrology: Principles, Models, and Applications.' 1st edn. 180 p. (CRC Press: Boca Raton, FL, USA)

HyQuest Solutions (2018) TB6 Rain Gauge. Available at https://www.hyquestsolutions.com.au/fileadmin/user_upload/TB6_Brochure.pdf [accessed 24 September 2024]

Iowa State University (2025) Iowa Environmental Mesonet. Available at https://mesonet.agron.iastate.edu/lsr/ [accessed 10 January 2025].

Jorgensen DP, Hanshaw MN, Schmidt KM, Laber JL, Staley DM, Kean JW, Restrepo PJ (2011) Value of a dual-polarized gap-filling radar in support of southern California post-fire debris-flow warnings. *Journal of Hydrometeorology* **12**(6), 1581–1595. doi:10.1175/JHM-D-11-05.1

Kalogiros J, Anagnostou MN, Anagnostou EN, Montopoli M, Picciotti E, Marzano FS (2014) Evaluation of a new polarimetric algorithm for rain-path attenuation correction of X-band radar observations against disdrometer. *IEEE Transactions on Geoscience and Remote Sensing* **52**, 1369–1380. doi:10.1109/TGRS.2013.2250979

Kean JW, Staley DM, Cannon SH (2011) In situ measurements of post-fire debris flows in southern California: comparisons of the timing and magnitude of 24 debris-flow events with rainfall and soil moisture conditions. *Journal of Geophysical Research: Earth Surface* **116**, F04019. doi:10.1029/2011JF002005

Khan MR, Gourley JJ, Duarte JA, Vergara H, Wasielewski D, Ayral PA, Fulton JW (2021) Uncertainty in remote sensing of streams using noncontact radars. *Journal of Hydrology* **603**, 126809. doi:10.1016/j.jhydrol.2021.126809

Krabbenhoft CA, Allen GH, Lin P, Godsey SE, Allen DC, Burrows RM, DelVecchia AG, Fritz KM, Shanafield M, Burgin AJ, Zimmer MA (2022) Assessing placement bias of the global river gauge network. *Nature Sustainability* **5**(7), 586–592. doi:10.1038/s41893-022-00873-0

Kumjian MR, Khain AP, Benmoshe N, Ilotoviz E, Ryzhkov AV, Phillips VTJ (2014) The anatomy and physics of ZDR columns: investigating a polarimetric radar signature with a spectral bin microphysical model. *Journal of Applied Meteorology and Climatology* **53**, 1820–1843. doi:10.1175/JAMC-D-13-0354.1

Kumjian MR, Lebo ZJ, Ward AM (2019) Storms producing large accumulations of small hail. *Journal of Applied Meteorology and Climatology* **58**, 341–364. doi:10.1175/JAMC-D-18-0073.1

Maddox RA, Zhang J, Gourley JJ, Howard KW (2002) Weather radar coverage over the contiguous United States. *Weather and Forecasting* **17**, 927–934. doi:10.1175/1520-0434(2002)017 < 0927:WRCOTC > 2.0.CO;2

Moody JA, Shakesby RS, Robichaud PR, Cannon SH, Martin DA (2013) Current research issues related to post-wildfire runoff and erosion processes. *Earth Science Reviews* **122**, 10–37. doi:10.1016/j.earscirev.2013.03.004

MTBS (2020) Monitoring Trends in Burn Severity Data Access. (USDA Forest Service and US Geological Survey) Available at http://mtbs.gov/

NASA/METI/AIST/Japan Spacesystems and US/Japan ASTER Science Team (2009) ASTER Global Digital Elevation Model [Dataset]. NASA EOSDIS Land Processes Distributed Active Archive Center. [accessed 1 October 2025] doi:10.5067/ASTER/ASTGTM.002

National Weather Service (2025) La Veta Mountain, La Veta Pass. Available at https://www.weather.gov/wrh/timeseries?site = KVTP [accessed 10 January 2025]

Neary GD, Leonard MJ (2019) Physical Vulnerabilities from Wildfires: Flames, Floods, and Debris Flows. In 'Natural Resources Management and Biological Sciences'. (Eds ER Rhodes, H Naser) pp. 581–603. (IntechOpen) doi:10.5772/intechopen.87203

NOAA Multi-Radar/Multi-Sensor System (MRMS) (2024) Operational Product Viewer. Available at https://mrms.nssl.noaa.gov/qvs/product_viewer/index.php?time_mode = update&zoom = 7&clon = -97&clat = 28&product_type = crefls&product = CREF [accessed 7 February 2024]

NOAA-USGS Debris Flow Task Force (2005) NOAA-USGS Debris-Flow warning system – final report 1283, 47 p. (US Geological Survey) doi:10.3133/cir1283

Osborne AP, Zhang J, Simpson MJ, Howard KW, Cocks SB (2023) Application of machine learning techniques to improve Multi-Radar Multi-Sensor (MRMS) precipitation estimates in the western United States. *Artificial Intelligence for the Earth Systems* **2**, 220053. doi:10.1175/AIES-D-22-0053.1

Parks SA, Abatzoglou JT (2020) Warmer and drier fire seasons contribute to increases in area burned at high severity in western US Forests From 1985 to 2017. *Geophysical Research Letters* **47**, e2020GL089858.

Parsons A, Robichaud PR, Lewis SA, Napper C, Clark JT (2010) Field guide for mapping post-fire soil burn severity. Gen. Tech. Rep. RMRS-GTR-243. 49 p. (USDA Forest Service, Rocky Mountain Research Station: Fort Collins, CO)

QGIS Development Team (2024) QGIS Geographic Information System. (Open Source Geospatial Foundation Project) Available at http://qgis.osgeo.org.

Rengers FK, McGuire LA, Kean JW, Staley DM, Hobley DEJ (2016) Model simulations of flood and debris flow timing in steep catchments after wildfire. *Water Resources Research* **52**(8), 6041–6061. doi:10.1002/2015WR018176

Staley DM, Negri JA, Kean JW, Laber JL, Tillery AC, Youberg AM (2017) Prediction of spatially explicit rainfall intensity–duration thresholds for post-fire debris-flow generation in the western United States. *Geomorphology* **278**, 149–162. doi:10.1016/j.geomorph.2016.10.019

United States Census Bureau (2020) La Veta town, Colorado. Available at https://data.census.gov/profile/La_Veta_town,_Colorado?g=160XX00US0844100) [accessed 10 January 2025]

US Geological Survey (2020) USGS water data for the Nation. (US Geological Survey National Water Information System database) [accessed 1 October 2021] doi:10.5066/F7P55KJN

USGS (2009) 'Collection, Quality Assurance, and Presentation of Precipitation Data.' US Geological Survey Office of Surface Water Technical Memorandum No. 2006.01.

USGS Post-Fire Debris Flow Hazard Assessment Viewer (2025) Available at https://usgs.maps.arcgis.com/apps/dashboards/c09fa874362e48a9afe79432f2efe6fe [accessed 10 January 2025]

Wang Y, Chandrasekar V (2009) Algorithm for estimation of the specific differential phase. *Journal of Atmospheric and Oceanic Technology* **26**, 2565–2578. doi:10.1175/2009JTECHA1358.1

Westerling AL, Hidalgo HG, Cayan DR, Swetnam TW (2006) Warming and earlier spring increase western US forest wildfire activity. *Science* **313**, 940–943. doi:10.1126/science.1128834

Zhang J, Howard K, Langston C, Kaney B, Qi Y, Tang L, Grams H, Wang Y, Cocks S, Martinaitis S, Arthur A, Cooper K, Brogden J, Kitzmiller D (2016) Multi-Radar Multi-Sensor (MRMS) quantitative precipitation estimation: initial operating capabilities. *Bulletin of the American Meteorological Society* **97**, 621–638. doi:10.1175/BAMS-D-14-00174.1

Zhang J, Tang L, Cocks S, Zhang P, Ryzhkov A, Howard K, Langston C, Kaney B (2020) A dual-polarization radar synthetic QPE for operations. *Journal of Hydrometeorology* **21**, 2507–2521. doi:10.1175/JHM-D-19-0194.1

Data availability. The data used to generate the results in the paper are available in the following locations. Precipitation, river surface velocity and river stage measurements collected on the Spring Creek burn area by the US Geological Survey are available from (Hempel *et al.* 2025): 10.5066/P133XUDC. The MRMS data that were used in this study were obtained from the NWS operational data feed archived by the publicly accessible Iowa Environmental Mesonet by Iowa State: https://mesonet.agron.iastate.edu/archive/. The NOXP radar data were provided in the raw Sigmet format (Gourley 2024) as well as the operator logs (Gourley 2025).

Conflicts of interest. The authors declare no conflicts of interest, and the funders had no role in the design of the study, in the collection, analyses, or interpretation of data, in the writing of the manuscript, or in the decision to publish the results.

Declaration of funding. Funding for the US Geological Survey component of the post-fire hydrometeorological observatory was provided by the Colorado State Department of Transportation. The deployment of the NOXP radar was supplied by the NOAA/National Severe Storms Laboratory. Additional funding was provided by NOAA/Office of Oceanic and Atmospheric Research under NOAA-University of Oklahoma Cooperative Agreement #NA21OAR4320204, US Department of Commerce. Their support of this research endeavor is greatly appreciated. Any use of trade, firm, or product names is for descriptive purposes only and does not imply endorsement by the US Government.

Acknowledgements. Internal reviews were provided by Jorge Duarte (Cooperative Institute for Severe and High-Impact Weather Research and Operations and NOAA National Severe Storms Laboratory), Brian Ebel (USGS) and Diana Zamora-Reyes (USGS). Their commentaries and suggested revisions greatly improved the quality of the manuscript. We also recognize journal-provided reviews by David B. Cavagnaro, California Geological Survey, and an anonymous reviewer that enhanced the quality, clarity and accessibility of the manuscript.

Author affiliations

[A]NOAA/National Severe Storms Laboratory, Norman, OK, USA.

[B]Advanced Radar Research Center, University of Oklahoma, Norman, OK, USA.

[C]Civil and Environmental Engineering, University of Wisconsin–Madison, Madison, WI, USA.

[D]United States Geological Survey, Denver, CO, USA.

[E]Cooperative Institute for Severe and High-Impact Weather Research and Operations, University of Oklahoma, Norman, OK, USA.